Origin of scattering defect observed in large diameter Ti:Al2O3 crystals grown by the Kyropoulos technique

G. Sen, Guillaume Alombert-Goget, V. Nagirnyi, I. Romet, T.N. Tran Caliste, J. Baruchel, J. Muzy, L. Giroud, K. Lebbou, Th. Duffar

Journal Pre-proofs

Origin of scattering defect observed in large diameter Ti:Al_2O_3 crystals grown by the Kyropoulos technique

G. Sen, G. Alombert Goget, V. Nagirnyi, I. Romet, T.N. Tran Caliste, J. Baruchel, J. Muzy, L. Giroud, K. Lebbou, Th. Duffar

PII: S0022-0248(20)30053-1
DOI: https://doi.org/10.1016/j.jcrysgro.2020.125530
Reference: CRYS 125530

To appear in: *Journal of Crystal Growth*

Received Date: 23 September 2019
Revised Date: 12 December 2019
Accepted Date: 26 January 2020

Please cite this article as: G. Sen, G. Alombert Goget, V. Nagirnyi, I. Romet, T.N. Tran Caliste, J. Baruchel, J. Muzy, L. Giroud, K. Lebbou, Th. Duffar, Origin of scattering defect observed in large diameter Ti:Al_2O_3 crystals grown by the Kyropoulos technique, *Journal of Crystal Growth* (2020), doi: https://doi.org/10.1016/j.jcrysgro.2020.125530

Origin of scattering defect observed in large diameter Ti:Al_2O_3 crystals grown by the Kyropoulos technique

G. Sen[1], G. Alombert Goget[2], V. Nagirnyi[3], I. Romet[3], T. N. Tran Caliste[4], J. Baruchel[4], J. Muzy[1, 5], L. Giroud[1], K. Lebbou[2], Th. Duffar[1]

[1]Univ. Grenoble Alpes, CNRS, Grenoble INP*, SIMAP, Grenoble, France

[2]Institut Lumière Matière, UMR5306 Université Lyon1-CNRS, 69622, Villeurbanne, France

[3]Institute of Physics, University of Tartu, W. Ostwald str. 1, 50411 Tartu, Estonia

[4]ESRF, BP 220, 38043 Grenoble, France

[5]RSA le rubis SA, BP 16, 38560 Jarrie, France

Corresponding author: T. Duffar, e-mail: thierry.duffar@grenoble-inp.fr

* Institute of Engineering, Univ. Grenoble Alpes

Abstract

Large diameter Ti-doped sapphire single crystals grown by the Kyropoulos technique along the A-axis, show detrimental light scattering close to the central C-plane. Thermo-luminescence measurements evidence that this defect is associated to a high level of oxygen vacancies. X-ray topography and Rocking Curve Imaging were performed. They show that the dislocation number is very small where scattering occurs, compared to the rest of the crystal, in agreement with results of numerical modelling of thermo-elastic stresses during crystal growth. A model is proposed in order to explain the scattering effect, based on the precipitation of nano-voids from vacancies in the absence of dislocations.

Keywords

A1. Line defects A1. Stresses A1. Computer simulation A1. X-ray topography

A2. Kyropoulos method B1. Sapphire B3. Solid state lasers

I INTRODUCTION

The excellent mechanical, thermal and optical properties of titanium doped sapphire (Ti:Al_2O_3) allow the development of laser systems with very high average and peak powers. Doping sapphire with Ti^{3+} provides a broad emission band, giving rise to tunable lasers of wavelength in the range 660–1180 nm and producing lasers of pulses less than 10 fs [1, 2]. This amplifier material is currently the most widely used in pW-fs laser chains based on the chirped pulse amplification (CPA) technique [3]. Development of these high-power laser systems opens the way to applications based on portable relativistic laser-electron accelerators [4] or on laser-driven ion sources [5]. New projects aiming to obtain power about tens or hundreds of pW are under development. Such objectives require crystals with large diameter and high quality, almost without defects, with relatively high concentration of dopant.

We have shown that 100 mm diameter sapphires obtained by the Kyropoulos method have the required properties to produce high efficiency lasers and amplifiers [6, 7]. In a preceding paper [8], members of our team observed and discussed an optical defect responsible for light scattering in large-diameter Ti:Al_2O_3 crystals grown by this Kyropoulos technique along the A-axis. As can be shown on figures 1-a) and 1-b), this defect is clearly visible by naked eyes, under lateral illumination. It has been called “Milky Defect” because it appears as a transversal band along the diameter of crystal slices, looking like Milky Way. It was established that:

- The Milky Defect is always along the full diameter of the disks and perpendicular to the C-axis i.e. the Milky Defect is along the C-plane. Its thickness is 5 to 10 millimeters and it

presents sharp edges. It begins a few centimeters after the seed and expands all along the crystal. It never appeared in crystals pulled along the C-axis.

- It is not related to bubbles, as none was observed by optical- nor scanning or transmission electron-microscopy. Sapphire samples were always very good single crystals without twin, grain boundary or significant misorientation.

- Scattering sensitivity to incident light polarization and illumination direction (with respect to crystallographic axes) suggests that the scattering elements are not spherical and have a preferred orientation versus the crystal axes.

- The blue luminescence, associated to the presence of Ti^{4+} ions, decreases in the Milky Defect. This could be associated to oxygen deficiency in this region of the crystals.

- This scattering effect induces transmittance losses, decreases the Figure of Merit of the crystals and induces a loss of 22% of the slope laser efficiency measured inside the Milky Defect, compared to the rest of the sample. The result is that such defective samples cannot be used in a laser cavity.

Evidence for sub-micrometer inclusions in titanium doped sapphire crystals grown by the Czochralski technique along the A-axis has been reported earlier and they have been found to form colonies oriented along the C-plane [9, 10]. Evidence for faceted voids in the range of 20 nm – 30 nm arranged along the C-plane has also been reported for undoped sapphire crystals grown by the EFG technique [11]. In both cases, the voids have been determined to be formed due to high concentration of oxygen vacancies generated by the reducing atmosphere in the furnace containing carbon elements. In the case of undoped sapphire crystals grown by the HEM technique there are interferogram images of A-plane discs showing a linear band of perturbed wave transmission not observed in the C-plane or M-plane discs [12]. Although the orientation of this linear perturbed band is not mentioned in the paper, it passes exactly through

the center so that it looks like a Milky Defect as observed in our samples. It follows from these results that the Milky Defect zone occurrence may not be exclusive to just titanium-doped nor Kyropoulos-grown sapphire crystals.

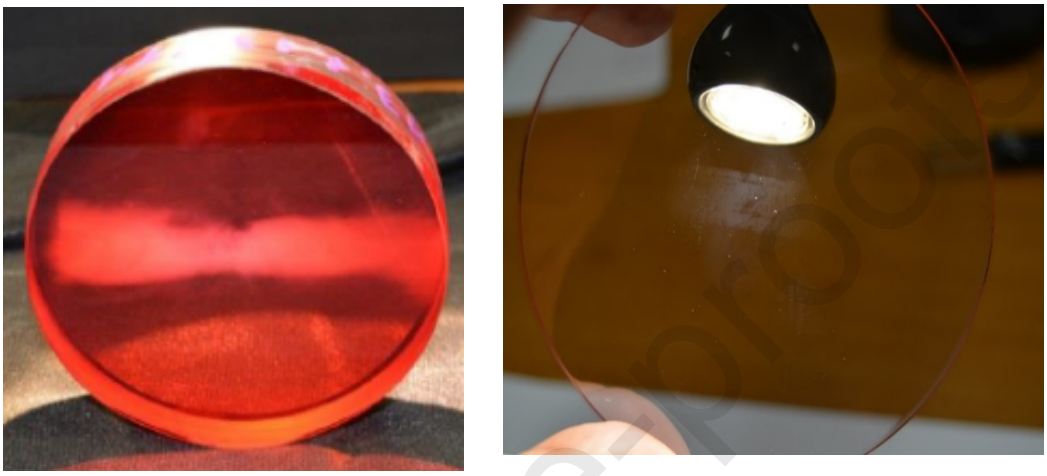

(a) *(b)*

Figure 1 : Ten cm diameter Ti:Al_2O_3 disks under lateral illumination. The A-axis (pulling direction) is perpendicular to the disks and the C-axis points upward. (a) 10 mm thick disk (from[8]) ; (b) 1mm thick disk.

By merging these bibliographic details and our previous results, it can be concluded that the Milky Defect is due to non-spherical nano-voids 30 to 100 nm in size and likely to be associated to oxygen deficiencies, as described by Danko *et al.* for larger particles [13]. Such potential oxygen deficiency, in our crystals, could be related to the contact of the melt with the reducing Mo crucible and to the gas atmosphere that is even more reducing, due to the presence of massive graphite parts in the heating and insulating materials in the furnace. The scattering effect can be explained by the phenomenon of Tyndall scattering of light from sub-micrometer size inclusions which are non-spherical in shape [10, 14].

However, the origin of these particles remains unknown. The reason of their location in a one-centimeter thick plate located all along the full diameter of the crystals and perpendicular to the C-axis is particularly mysterious. The present paper aims to describe further experimental and numerical results suggesting a mechanism for the origin of the Milky Defect.

II EXPERIMENTAL

II-1 Sample preparation

A crystal was grown by the Kyropoulos method along the A-axis in a Cyberstar furnace from the company RSA, see [15, 16] for further details on the growth conditions. The crystal was weighing around 6 kg with an average diameter of 11 cm and devoid of any visual macro- and microscopic defect like bubble or inclusion. It is representative of the regular production of Ti:Al_2O_3 in this company and presented the Milky Defect. Two horizontal circular discs were cut from the upper half of the crystal (see figure 1 in [15] for crystal shape and cut location). These discs had their face perpendicular to the A-axis; diameter was 100 mm and thicknesses 0.5 and 1 mm. Various samples were cut from Milky and non-Milky regions in these discs. All samples used for the analyses discussed in the work were chemo-mechanically polished according to the RSA company procedure.

II-2 Characterization of point defects

Two smaller disc samples were prepared from the Milky and non-Milky zones with dimensions of 10 mm in diameter and 1 mm in thickness. Thermoluminescence (TSL) measurements of the irradiated samples were performed in a Janis VPF-800 cryostat. An X-ray tube (W_{anode} 40 kV, 10 mA) was used for sample irradiation at room temperature for 5 minutes providing a dose rate approximately 20 $Gy.s^{-1}cm^{-2}$. TSL curves were recorded using a Hamamatsu H8259 photon counting head in the temperature interval of 295-700 K at a heating rate of 10 K/min. The TSL spectrum was repeatedly measured for 60 s using an ARC SpectraPro 300i grating

monochromator equipped with a CCD detector with a spectral sensitivity in the range of 190–1100 nm. Considering the given heating rate, each emission spectrum was measured within a temperature interval of 10 K. This allowed measuring several spectra in the temperature range of each TSL peak. To obtain the full spectrum in the range 200-900 K the spectra recorded for different spectral regions were normalized in the overlapping parts and stitched together. TSL glow curves were corrected by subtracting the background signal of an empty sample holder, consisting of the blackbody emission and dark counts of the detector. TSL emission spectra were corrected for the monochromator spectral efficiency and spectral sensitivity of the detector.

Figure 2 (a) shows normalized TSL curves recorded from the two samples. For both samples, a prominent TSL peak at 415 K is registered. Its half-width (FWHM) is 34 K, and according to the accepted classification, it is a narrow one [17]. For the Milky Defect sample, the peak intensity at 415 K is 2.5 times higher than that for the transparent one.

For both Milky and non-Milky samples, various TSL emission spectra were recorded during the sample heating from 357 K to 547 K. In each glow peak, they feature three emission bands peaking at 330 nm, 430 nm, and 770 nm as shown in figure 2 (b). The emission band peaking at 330 nm is related to the F^+ centres, the band at 430 nm is associated with the emission of F centres, and the intense near-infrared band peaking at 770 nm is due to the $^2E \rightarrow {}^2T_2$ radiative transitions of the Ti^{3+} ions [17, 18]. The latter demonstrates a noteworthy mismatch with the positions of the Ti^{3+}-related band (730 nm) reported in some earlier papers (see, e.g., [19]), but those were given for the spectra which were not corrected for the instrumental response of the detection system. The F and F^+ centres are oxygen vacancies occupied by two and one trapped electron, respectively [20]. Supposedly, the emission of F^+, F and Ti^{3+} centres emerges in the TSL of irradiated samples due to the trapping of electrons thermally released from deep electron traps [17] correspondingly by oxygen vacancies, F^+ centres and Ti^{4+} ions. One of the latest

model of the corresponding processes is described for the oxygen-deficient α-Al_2O_3 in [21]. The shapes of the TSL spectra are practically identical for both Milky and non-Milky samples, while the emission intensity of the non-Milky sample is substantially weaker. This undoubtedly indicates a much higher concentration of oxygen vacancies in the Milky Defect than in the rest of the crystal.

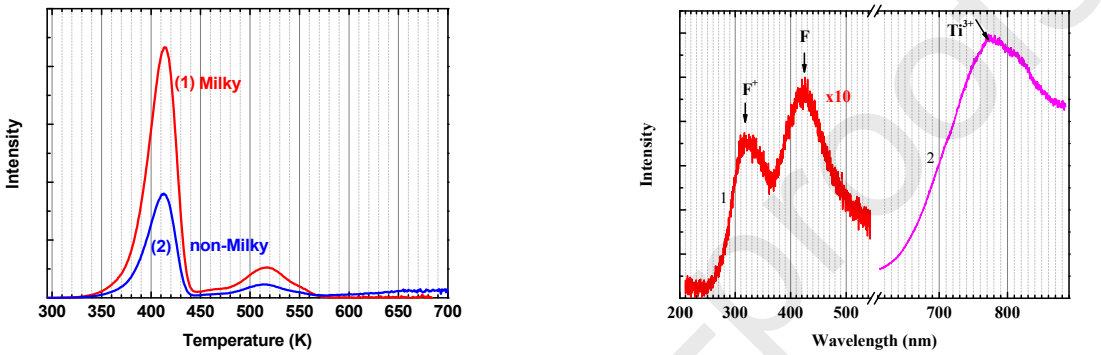

Figure 2: (a) TSL glow curves obtained from Milky (1) and non-Milky (2) zone of a Al_2O_3:Ti sample irradiated by X-rays with the dose rate of 20 $Gy.s^{-1}cm^{-2}$. *(b) TSL emission spectra measured in the region of 387-432 K (1) and 410-420 K (2).*

II-3 Characterization of dislocations

Projection X-Ray transmission topography was carried out at the BM05 beamline of the European Synchrotron Research Facility (ESRF) in Grenoble. A polychromatic (6-100 keV) extended beam (40 mm × 15mm) impinges on the crystal, which produces a Laue pattern. Each of the diffracted spots exhibits contrasts that reveal the perturbations of the crystallographic planes inside the crystals. This is because the incident synchrotron beam has a very low divergence, the angular width of the beam reaching a given point of the sample being in the μradian range. Therefore, all defects, such as dislocations, inclusions, stress field, twins and so on, present in the volume illuminated by the incident beam, are visualized on the beam spot.

The resolution of the technique is limited by the photographic film grain, of the order of one micrometer. Details of the X-Ray topography techniques used, as well as results concerning the global characterization of the crystals, are given in [15]. Dislocations were found to be the main type of defect in the samples and the average dislocation density was in the range of $<10^3$ in the center of the disc to $<10^5$ cm^{-2} at the periphery. These results were also confirmed with etch pit density measurements (10 min. in molten KOH [22]) giving around 500 cm^{-2} in the center of the crystals. The dislocation density increased from the center of the crystal to the outside. Here we focus only on the specificities of the dislocation patterns observed in the Milky Defect, compared to the rest of the sample.

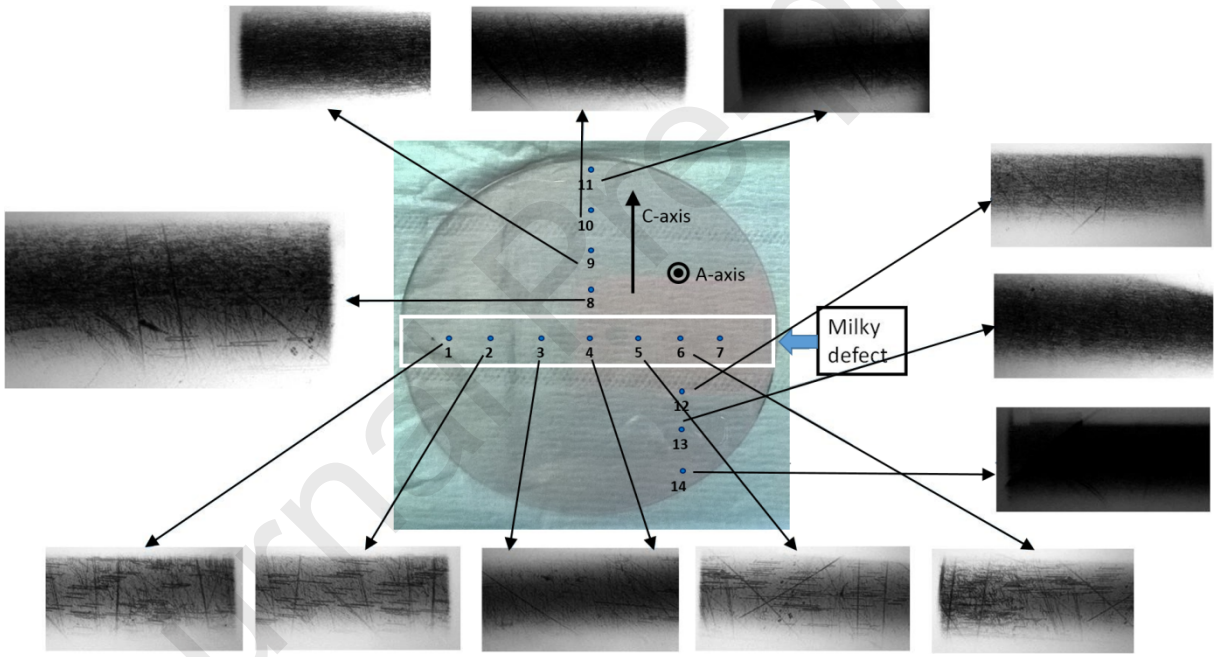

Figure 3: Points of analysis and Bragg spots diffracted by the (0001) type planes in transmission mode. Each spot shows 40 mm × 15mm of the sample.

The Bragg spots diffracted by the (0001)-type planes obtained for various regions of the circular sample are presented in figure 3. From these images, it is clear that there is a distinction in the dislocation behavior in the Milky Defect, compared to the rest of the disc. For the Milky region, dislocations are very distinct, parallel to each other and oriented along the C-plane. In this

region, the dislocation density gradually increases from the center of the sample to radially outwards. It will be shown later in the section that they correspond to the basal slip system, where there are only three dislocation directions. So that, it is sensible to estimate that, at a maximum, one third of dislocations could not be seen in the figure 3 in case their Burgers vector would be perpendicular to the diffraction vector. In conclusion, the dislocation density remains remarkably small in the Milky Defect zone.

When passing outside the Milky zone, there is a sharp increase in the dislocation density and the dislocations are entangled and not clearly oriented as in the milky zone, but once again they increase radially outwards and their density is much higher than in the Milky Defect region.

The most interesting dislocation pattern is observed for point 8 (middle left of figure 3) and magnified on Figure 4. This point is very close to the milky zone defect region and hence the dislocation pattern here shows two distinct behaviors. The lower part which is closer to the Milky zone shows the presence of oriented individual dislocations parallel to the C-plane, while the upper part shows a mesh of entangled dislocations as in the rest of the crystal. This shows that there is a sharp demarcation between the Milky Defect and the rest of the crystal, with respect to dislocations. This is in accordance with the sharp boundary seen optically (Figure 1).

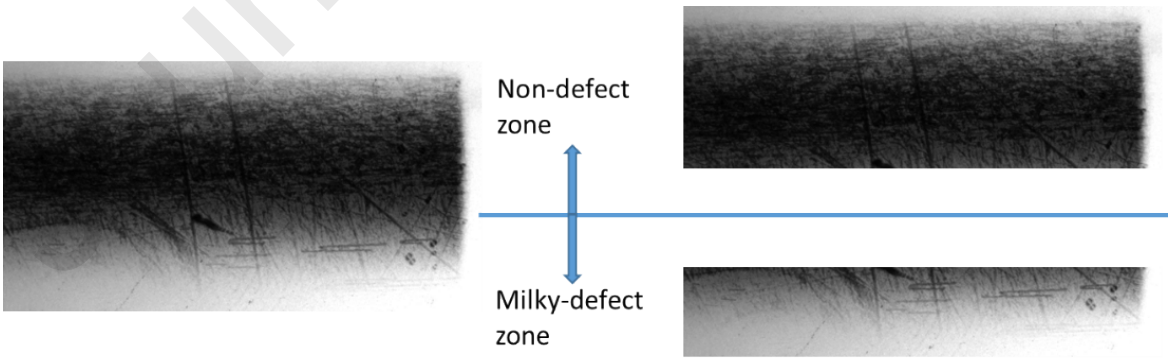

Figure 4: Transition of dislocation behavior between Milky Defect and non-defective zone observed for point 8 in figure 3.

In order to get more quantitative information on the dislocation patterns, Rocking Curve Imaging (RCI), which allows measurement of the spatial distribution of local lattice distortions [23], was also perform on the ESRF-BM05 beam line, in both projection [24] and section [25] modes. Two rectangular samples, 30 mm x10 mm were cut in one disc, such that the milky zone passes through their center. Details of the RCI experimental achievement and parameters are given in [16].

Maps were recorded in both projection and section modes for the C-plane (0006) reflection of the two samples. Maps were also recorded for the A-plane ($11\bar{2}0$) reflection of one sample in projection mode. Figure 5 gives a representative result in terms of mapping collected at the transition between the Milky Defect and the rest of the crystal.

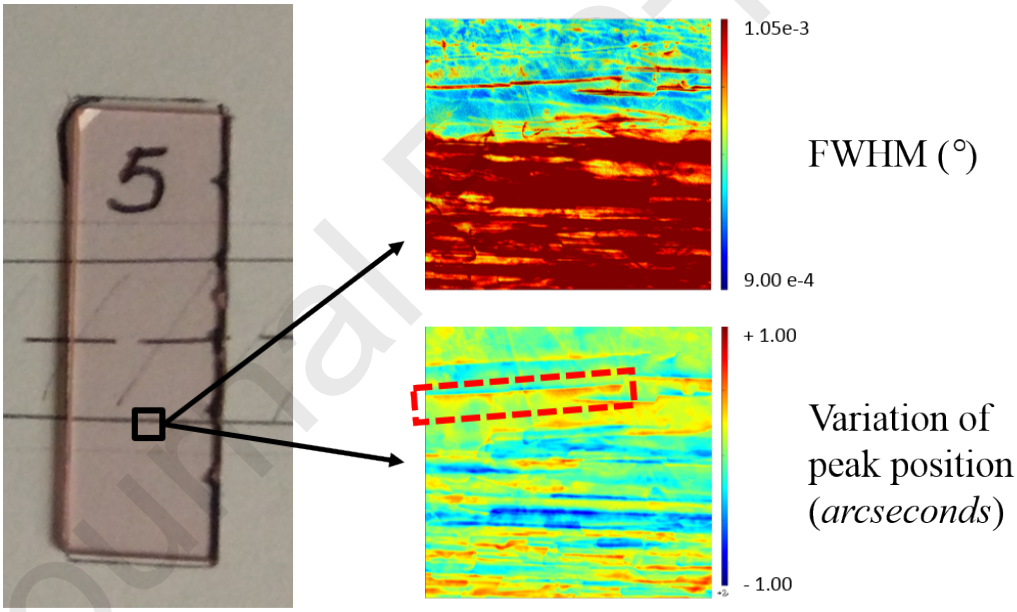

Figure 5: C-plane (0006) reflection in the transition zone (small black square) below the Milky Defect (delimitated by horizontal lines). Figures represent projection mapping of Full Width at Half Maximum (top) and variation of peak position (bottom).

Comparing mapping obtained in various locations on the samples [16], several results are assessed. In the middle of the Milky Defect zone in the first sample located at the center of the

disk, we do not see any dislocation in the section images. A ripple effect is seen instead (shown in [16]): interference fringes known as Kato fringes, which are signature of the extremely high crystalline quality at these positions, are observed [26]. The second sample, which is farther away from the center of the disc, shows some dislocations in the Milky Defect.

There is a sharp increase in the observed dislocations as soon as we progress into the non-Milky zone, as seen from the projection mapping of FWHM on Figure 5. A-plane ($11\bar{2}0$) reflection confirms that there are very few dislocations in the Milky Defect and they are horizontal. In the rest of the sample, there are numerous dislocations oriented in various directions. The difference in peak position between the two zones (~1 arcsec) suggests a lattice parameter variation of the order 10^{-5}.

The variation of Bragg angle when going from one side of the dislocation to the other side is given by [26]:

$$\partial\theta_B = \frac{b_r}{\pi r_d}$$

The peak position map for projection seen on figure 5 was used to measure the Burgers vector b_r of the marked dislocation. Knowing the dimensions of the image as scaled and using the color scale for the angle variation, the values of r_d (dislocation radius) and θ_B (angle variation) are 0.02 mm and 1.5 arc.sec. Thus, the Burgers vector for the marked dislocation was determined to be 4.57 Å. This value is very close to the lattice parameter, a = 4.76 Å, showing that the dislocations are due to slip of the C-planes in the A-axis directions. Considering that the analyzed dislocation belongs to the milky defect zone, it is concluded that the Milky Defect contains only dislocations formed by the basal slip. By the way, the basal slip in sapphire crystal has the lowest critical resolved shear stress at elevated temperatures: some tens of MPa, based on data obtained from deformation experiments [27].

III NUMERICAL MODELLING OF STRESSES IN THE GROWING CRYSTAL

The finite element software COMSOL-Multiphysics® was used for modelling the Kyropoulos growth of the Ti-doped sapphire crystals of interest. The model and the results are already published, in terms of temperature field and solid-liquid interface shape [28], Ti segregation [29] and stresses in the growing crystal. The reader may refer to figure 3 in [30] where a von Mises stress map in the growing crystal is shown, as well as stress variation along the crystal radius at several crystal lengths. Here, we focus our attention on the results of stress calculations with a more detailed analysis of the stress field shown in the aforementioned figure. As the dislocations of interest in the Milky Defect are belonging to the basal slip (section II-3), projection of the stress components on the C-plane are computed along the A-axes in order to check whether basal slip was activated or not.

In an axisymmetric approximation, the stress components are the normal stress in the radial direction (σ_r), the normal stress in the azimuthal direction (σ_φ), the normal stress in the axial direction (σ_z) and the shear stress (σ_{rz}). The shear stress has a very small projection on the C-plane and hence does not contribute to the basal slip. The radial distribution of three main normal stresses and their projection on the C-plane along the A-axis direction for one transversal half-section of the growing crystal and are shown on figure 6.

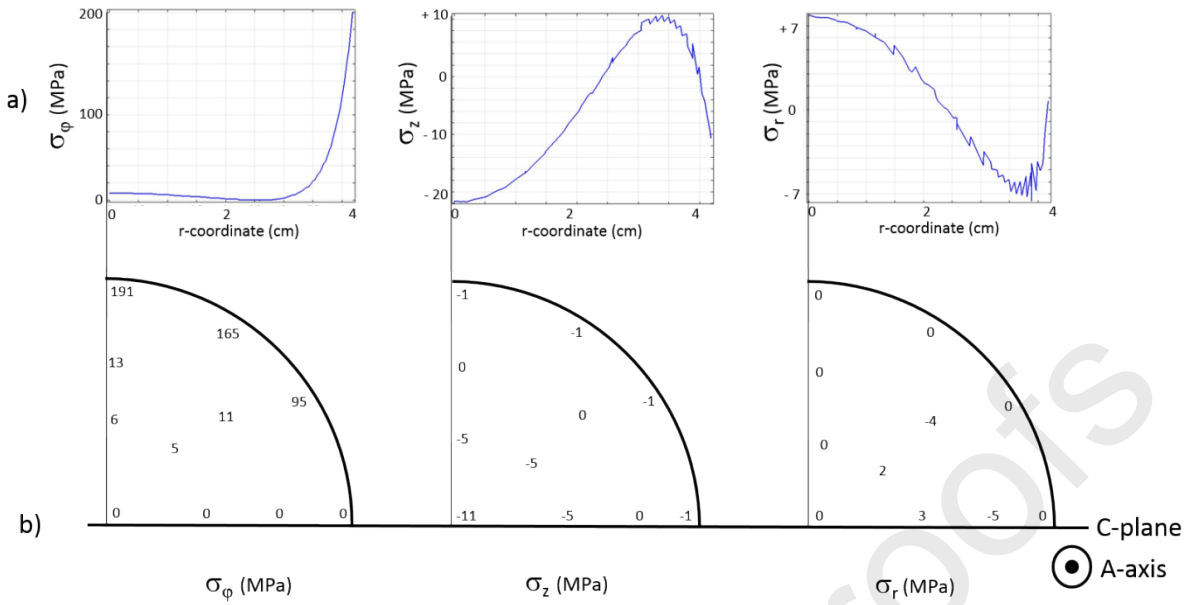

Figure 6: Stress component analysis at x=12cm position on figure 3 in [30]. a) Radial distribution of the three main stress components. b) Quarter-disk (A-plane) respective projections on the C-plane/A-axis basal slip system.

At this location and at this moment during the growth, it appears that the radial and axial stresses have low absolute values (respectively 7 and 22 MPa) and hence low projection values on the basal slip system. Similar treatments at other positions along the crystal show that these projections remain always lower than 20 to 30 MPa. Only the azimuthal component has high values (up to 200 MPa) with projections exceeding significantly the basal slip yield point. However, its projection is strictly null on the diametric C-plane, where it is oriented perpendicularly.

It follows that the stress responsible for the basal slip, which is the sum of the three component projections, is definitely not axi-symmetrical: the maximum stress values on the region along the central C-axis are much higher than the values on the region close to the central C-plane where it does not exceed significantly the critical resolved shear stress. This leads to a lower dislocation density along the central C-plane region corresponding to the Milky Defect as experimentally observed.

These stress calculations for the basal slip mechanism were carried out at the location where von Mises stress is maximum, but only for a particular instant during the crystal growth. To have a completely reliable point of view, it would be needed to have the maximum stress component values for basal slip for the whole growth process. Anyhow, this study shows that the most important stress component is the azimuthal one, which cannot activate the basal slip along the central C-plane.

IV DISCUSSION

To all the characterization efforts and results obtained, the following arguments can be added:

- High-temperature growth of sapphire crystals in a crystallization chamber composed of graphite and molybdenum elements takes place in a reducing atmosphere. This leads to the surface reduction of sapphire in contact with the Mo crucible and the atmosphere and generation of oxygen vacancies [11, 13]. Additionally. in the case of Ti-doped sapphire with low concentration of Ti^{4+} there could be simultaneous formation of both aluminum and oxygen vacancies as proposed in [31]:

$$TiO_2 \xrightarrow{Al_2O_3} Ti_{Al}^{\circ} + 2O_O^{\times} + V_{Al}''' + V_O^{\circ\circ}$$

- A dislocation is generally subjected to a climbing force normal to its slip plane when the point defect concentration in the immediate vicinity of the dislocation is not in local equilibrium with the defect sources and sinks on the dislocation. Point defects such as vacancies may be absorbed at a dislocation, and the dislocation climbs in an attempt to establish local equilibrium by absorbing the point defect [32]. Indeed, dislocations act as sinks for point defects.

- In the case of Al_2O_3, it has been established that the diffusion of oxygen vacancies is slower than the aluminum vacancies by a factor of 1000 in the temperature range [1400-

1900°C] [33, 34, 35]. In the case of titanium doped Al_2O_3, it has been noticed that the oxygen vacancy diffusion decreases further [33, 36, 37]. Thus, it can be assumed that aluminum vacancies diffuse much easily than oxygen vacancies towards dislocations and get dissipated leaving a surplus of oxygen vacancies compared to possible aluminum vacancies in the lattice.

- There are not many sinks available for the slower diffusing oxygen vacancies in the Milky Defect, where dislocation density is low. Therefore, their concentration is high and, if exceeding the solubility limit, they can bind together and form nanovoids [13]. The higher vacancy concentration could be the origin of the 10^{-5} variation of lattice parameter between the two zones.

The results of TEM analysis of our samples was reported in [8] with no observation of any particle. Further TEM observations have been performed meanwhile on the same samples. Only one 10 nm particle was observed, in the sample from the Milky Defect (Figure 7). Its faceted shape and strong contrast with the matrix suggest that it is a nanovoid. This kind of particles are good candidate for Tyndall diffusion. On the other hand, SAXS experiments performed inside and outside the Milky Defect did not show any particular precipitate population. This, considering the characterization parameters, suggests either that the precipitates are larger than 50 to 100 nm, or that they have a small contrast with the matrix, as could be the case of the precipitation of Al-Al_2O_4 spinel complexes speculated by [13].

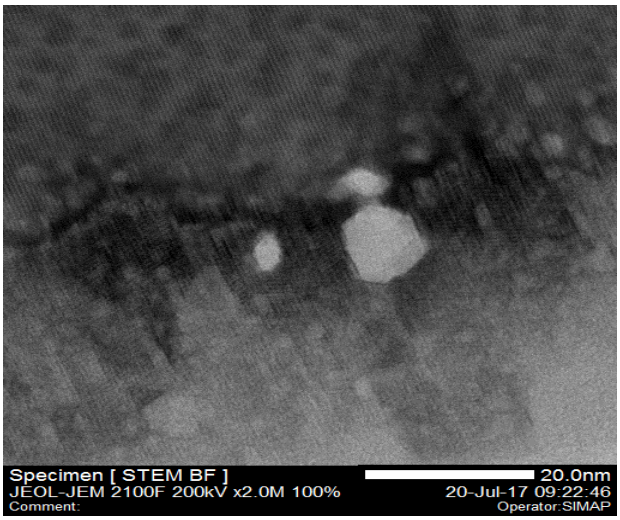

Figure 7: Faceted particle observed by TEM inside the Milky Defect region.

Finally, we propose the following hypothesis for the mechanism of formation and location of the Milky Defect:

1. The crystal grows at high-temperature in a furnace composed of many carbon-containing structures and in a Mo crucible. This creates a reducing atmosphere in the furnace and hence leads to formation of oxygen vacancies throughout the growing crystal.
2. During the growth there are thermal stresses acting on the crystal that can give rise to dislocations. However, thermal stresses responsible for basal slip dislocation generation are lower in a band along the C-plane passing through the center than in the rest of the sample. The critical resolved shear stress required for basal slip is barely reached in this region along the C-plane and hence there are very few dislocations in this region compared to the rest of the crystal.
3. Outside the central C-plane region, dislocations act as sinks for the point defects and hence attract most of the oxygen vacancies.
4. However, since there are very few dislocations in the region along the central C-plane there are not enough sinks for the oxygen vacancies in this region. These oxygen

vacancies start to bind together and aggregate to form voids in order to reduce the vacancy concentration to the solubility limit. Possibly, these voids take the shape of negative crystals and get faceted and oriented. Alternatively, the precipitates are composed of spinel-like Al-Al_2O_4 complexes.

5. Tyndall scattering of light from these precipitates situated along the central C-plane produces the Milky Defect.

Since similar phenomenon has also been observed in undoped sapphire, it can be deduced that titanium doping is not a predominant factor for this defect regime. However, it is possible that titanium doping enhances the mechanism of oxygen vacancy generation and void formation and that the red color it imparts to the crystal enhances the visibility of this defect.

IV CONCLUSION

The succession of phenomena as described above is the best-fit hypothesis for the explanation of the Milky Defect as it aggregates and satisfies most of the observations. However, it is not ascertained and cannot be taken as a definitive explanation for the defect formation. Hence, there is a need for further characterization and analysis for the samples. It is required to do a quantitative analysis of the laser light diffusion by the Milky Defect. From these measurements, it would be possible to calculate the dimensions of the features responsible for the diffusion of light and understand their shape factor with respect to the principle of Tyndall scattering [10]. It is important to compute numerically the thermal stress evolution during the full crystal growth process and then check for zones lower than the critical resolved shear stress. To confirm for the presence of possible voids in the Milky Defect, extensive TEM observations should also be performed, in parallel with Automatic Crystallography Orientation Mapping (ASTAR®) in order to characterize the precipitated phase and its orientation relation to the matrix.

In any case, this Milky Defect appears to be an excellent example of crystal defect interactions, as it involves growth atmosphere, dopant composition, point defects, crystallography, temperature gradient, stresses, dislocations and micro voids. It also reveals that the Kyropoulos process provides sapphire crystals of very good quality, but TOO good for the application. On the industrial point of view, in order to get rid of the Milky Defect, we can propose the following strategy with respect to our hypothesis. As oxygen vacancy-related precipitates are responsible of the defect, it is necessary to trap these vacancies inside dislocations. Therefore, larger stresses should occur in this region so that basal slip will be activated and create dislocations. The critical yield stress [27] is close to the calculated stresses in the central region (§ III), so that only a small increase of temperature gradient is likely to solve the problem, without generating unacceptable dislocation levels in the rest of the crystal. This is also supported by the rather small region occupied by the Milky Defect. Practically speaking, numerical simulation of heat transfer and stresses during growth would help suggesting optimized modifications of the insulation casing.

ACKNOWLEDGMENTS

This work has been performed in the frame of the FUI-TITANSaphir project funded by BPI and the Région Rhône-Alpes, we are grateful to the project coordinator N. Barthalay, from the RSA le Rubis company. The authors gratefully acknowledge the financial support of the Estonian Research Council (project PUT PRG111). Help of G. Renou and P. Donadieu for TEM analyses and of F. de Geuser for SAXS experiment was particularly appreciated. We also are indebted to C. Stelian for the numerical simulations of growth process. V. Kryvonosov, Institute for Single Crystals, Kiev, Ukraine, helped a lot with useful discussions and ideas.

REFERENCES

[1] Wall K. F., Sanchez A., The Lincoln Laboratory Journal 3 (1990) 447.

[2] Spence D. E., Kean P. N., Sibbett W., Opt. Lett. (1991) 42.

[3] Alombert-Goget G., Lebbou K., Barthalay N., Legal H., Chériaux G., Opt. Mater. 36 (2014) 2004.

[4] Esarey E., Schroeder C. B., Leemans W. P., Rev. Mod. Phys. 81 (2009) 1229.

[5] Macchi A., Borghesi M., Passoni M., Rev. Mod. Phys. 85 (2013) 751.

[6] Nehari A., Brenier A., Panzer G., Lebbou K., Godfroy J., Labor S., Legal H., Cheriaux G., Chambaret J.P., Duffar T., Moncorgé R. Crystal growth & design V 11 (2011) 445-448.

[7] Alombert-Goget G., Sen G., Pezzani C., Barthalay N., Duffar, T., Lebbou K., Opt. Mater. 61 (2016) 21.

[8] Alombert-Goget G., Guyot Y., Nehari A., Benamara O., Blanchard N., Brenier A., Barthalay N., Lebbou K., CrystEngComm 20 (2018) 412-419.

[9] Kryvonosov I. V., Lytvynov L. A., Crystallography Reports, 57 (2012) 967–973.

[10] Vyshnevskiy S.D., Kryvonosov Y. V., Lytvynov L.A., Functional Materials 13 (2006) 238–244.

[11] Borodin V. A., Ionov A. M., Yalovets T. N., J. Crystal Growth 104 (1990) 157–164.

[12] Smith M., Schmid K., Schmid F., Khattak C. P., Lambropoulos J., SPIE (1999) 85–92.

[13] Danko A. Y., Sidelnikova N. S., Adonkin G. T., Budnikov A. T., Nizhandovskii S. V., Krivonogov S. I., Crystallography Reports, 49 (2004) 294-299.

[14] Vyshnevskiy S.D., Kryvonosov E.V., Lytvynov L.A. Crystallography Reports 53 (2008) 154-157.

[15] Sen G., Caliste T. N. T., Stelian C., Baruchel J., Barthalay N., Duffar T., J. Crystal Growth 468 (2017) 477-483.

[16] Sen G. "Kyropoulos growth and characterization of titanium doped sapphire" PhD thesis, Univ. Grenoble Alpes, 11th January 2018.

[17] Kortov V., Lushchik A., Nagirnyi V., Ananchenko D., Romet I., J. Luminescence 186

(2017) 189–193.

[18] Mikhailik V. B., Kraus H., Wahl D. Appl. Phys. Lett. 86 (2005) 101909.

[19] Mikhailik V. B., Di Stefano P. C. F., Henry S., Kraus H., Lynch A., Tsybulskyi V., Verdier M. A. J. Applied Physics 109 (2011) 053116.

[20] Moroño A., Hodgson E. R., J. Nuclear Materials, 249 (1997) 128–132.

[21] Nikiforov S.V., Lushchik A., Nagirnyi V., Romet I., Ponomareva A.I., Ananchenko D.V., Moiseykin E.V. Radiation Measurements 122 (2019) 29-33.

[22] Vardiman R. G., J. Electrochem. Soc. 118 (1974) 1804-1809.

[23] Tran Thi T.N., Morse J., Caliste D., Fernandez B., Eon D., Härtwig J., Barbay C., Mer-Calfati C., Tranchant N., Arnault J. C., Lafford T. A., Baruchel J., J. Applied Crystallography 50 (2017) 561–569.

[24] Calamiotou M., Chrysanthakopoulos N., Papaioannou G., Baruchel J., J. Applied Physics 102 (2007) 083527.

[25] Pernot J., Volpe P. N., Omnès F., Muret P., Mortet V., Haenen K., Teraji T. Phys. Rev. B 81 (2010) 1–7.

[26] Tsoutsouva M. G., Oliveira V. A., Baruchel J., Camel D., Marie B., Lafford T. A., J. Applied Crystallography 48 (2015) 645–654.

[27] Lagerlof K. P. D., Heuer A. H., Castaing J., Riviere J. P., Mitchell T. E., J. Am. Ceramic Soc.77 (1994) 385–397.

[28] Stelian C., Sen G., Barthalay N., Duffar T., J. Crystal Growth 453 (2016) 90-98.

[29] Stelian C., Alombert-Goget G., Sen G., Barthalay N., Lebbou K., Duffar T., Optical Materials 69 (2017) 73-80.

[30] Stelian C., Sen G., Duffar T., J. Crystal Growth 499 (2018) 77-84.

[31] Rasmussen J., Kingery W. D., J. Am. Ceramic Soc. 53 (1970) 436–440.

[32] Thomson R. M., Balluffi R. W., J. Applied Physics, 33 (1962) 803–816.

[33] Lagerlof K. P. D., Mitchell T. E., Heuer A. H., J. Am. Ceramic Soc. 72 (1989) 2159–2171.

[34] Mitchell T. E., Hobbs L. W., Heuer A. H., Castaing J., Cadoz J., Philibert J., Acta Metallurgica 27 (1979) 1677–1691.

[35] Pletka B. J., Heuer A. H., Mitchell T. E., Acta Metallurgica, 25 (1977) 25–33.

[36] Haneda H., Monty C., J. Am. Ceramic Soc. 72 (1989) 1153–1157.

[37] Reddy K. P. R., Cooper A. R., J. Am. Ceramic Soc. 65 (1982) 634–638.

Highlights

1 – Explanation for scattering band is proposed

2 – There are very few dislocations in the scattering band

3 – This is explained by peculiarities of stress field during growth

4 – There are much more oxygen vacancies in the scattering band

5- Vacancies precipitate as nanovoids in the scattering band